Available online at www.sciencedirect.com
SCIENCE DIRECT®
Journal of Computational Physics 196 (2004) 348–366
JOURNAL OF COMPUTATIONAL PHYSICS
www.elsevier.com/locate/jcp

A collocated grid finite volume method for aeroacoustic computations of low-speed flows

Wen Zhong Shen *, Jess A. Michelsen, Jens Nørkær Sørensen

Department of Mechanical Engineering, Fluid Mechanics, Technical University of Denmark, Building 403, DK-2800 Lyngby, Denmark

Received 25 October 2002; received in revised form 14 August 2003; accepted 5 November 2003

Abstract

A numerical algorithm for simulation of acoustic noise generation, based on collocated grids, is described. The approach, that was originally developed using a viscous/inviscid decomposition technique, involves two steps comprising a viscous incompressible flow part and an inviscid or viscous acoustic part. On collocated grids the inviscid solution is found to be mesh dependent due to unavoidable extrapolations of the acoustic pressure and density at walls, differing from the case on staggered grids where no extrapolation is needed. The situation is most pronounced when a sharp body is considered. A viscous acoustic algorithm is proposed to overcome the difficulty. Numerical computations of flows past a circular cylinder and a NACA 0015 airfoil show that a viscous/viscous coupling is more natural and gives excellent results as compared to those obtained in previous computations based on viscous/inviscid coupling on staggered grids. The model is applied to the problem of an airfoil exposed to a gust and results are compared to the numerical results of Lockard and Morris [AIAA J. 36(6) (1998) 907].

AMS: 65M06; 76Q05; 76D05

Keywords: Navier–Stokes equations; Computational aeroacoustics; Collocated grid; Finite volume method

1. Introduction

Computational aeroacoustics (CAA) is now becoming a common tool for predicting noise generated from flows, such as helicopter, wind turbine and jet flows. Noise prediction codes can be divided into two categories. One is based on the Lighthill acoustic analogy [1] resulting in linearized wave equations combined with sound sources, such as monopoles, dipoles and quadrupoles [2–7] and the other is based on solving the compressible Euler/Navier–Stokes equations [8–13,15]. The former models establish direct relationship between noise sources and a far-field receiver. Since reflection and diffraction and other nonlinear interaction effects are not included in linear models, these models are used to predict far-field noise

* Corresponding author. Tel.: +45-4525-4317; fax: +45-4593-0663/454-588-2421.
E-mail address: shen@mek.dtu.dk (W.Z. Shen).

0021-9991/$ - see front matter © 2003 Elsevier Inc. All rights reserved.
doi:10.1016/j.jcp.2003.11.006

where non-linear effects can be neglected. The latter models employ a computational mesh surrounding all solid walls and solve the Euler/Naver–Stokes equations in a domain where non-linear effects are included. Due to limitation of computer resources, it is difficult to compute propagation over long distances and therefore these models are preferable to study near-field acoustics.

For near-field noise at high Mach numbers, Tam and coworkers [8,9] developed a compressible Euler/compressible Navier–Stokes coupling method. For low Mach number flows, Hardin and Pope [11] proposed a non-linear two step procedure for aeroacoustic computations which is suitable for both generation and propagation. Based on the pioneering work of Hardin and Pope, a general aeroacoustic model was recently developed by the authors for laminar and turbulent flows [13–15].

The developed scheme was based on staggered grids and works well for simple flows (cylinder flows and airfoil flows). For general non-orthogonal meshes, however, staggered techniques tend to become rather complex, either storing all velocity components on every cell face, or introducing derivatives of the grid curvature through Christoffel symbols. In order to avoid these difficulties, many researchers have investigated non-staggered methods. About 20 years ago, Rhie and Chow [16] proposed a procedure using a momentum based interpolation for the cell face mass fluxes in the continuity equation which closely imitates the staggered practice by letting mass conservation be expressed in terms of mass fluxes across cell interfaces. The mass fluxes are driven by 1δ pressure differences across the faces. Hence, velocity–pressure decoupling cannot occur. The Rhie–Chow procedure gives excellent results for steady-state flow problems where a large local time step is used. For unsteady flow calculation, however, when using small time steps, pressure oscillations may still appear. Recently, we have shown that spurious oscillations can be suppressed by changing the flux interpolation scheme [17] and that the technique can be further refined by using the SIMPLEC scheme to obtain faster convergence for steady computations as well as more consistent solutions for unsteady computations [18].

The focus of the paper is to develop a suitable method that is based on collocated grids for acoustic computations and to obtain smooth compressible solutions, which are primarily governed by the Euler equations, perturbed about an incompressible viscous flow.

The paper is organized as follows. In Section 2, the governing equations for flows and acoustic waves are given. The numerical implementation on collocated meshes is given in Section 3. Results for acoustic waves generated from flows past a circular cylinder and an airfoil are presented in Section 4.

2. Formulation of the problem

Based on the splitting approach introduced by Hardin and Pope [11], a numerical algorithm on staggered grids for acoustic noise generation was developed by Shen and Sørensen [14,15]. The algorithm consists of two steps comprising a viscous incompressible flow part and an inviscid acoustic part. In the present work, this approach has been further refined by also retaining the viscous terms in the acoustic set of equations, in the following referred to as perturbed equations. Indeed, it can be shown that numerical irregularities appearing near-solid boundaries can be attributed to the use of inviscid perturbed equations. On the other hand, retaining the viscous terms in the perturbed equations, the solution can be treated consistently everywhere by the splitting.

The basic flow equations are described in early publications [13–15], hence we only consider the perturbed equations. The basic formulation is based on the following decomposition of the compressible variables

$$u_i = U_i + u_i', \tag{1}$$

$$p = P + p', \tag{2}$$

$$\rho = \rho_0 + \rho', \tag{3}$$

where P, ρ_0 and U_i are the incompressible pressure, density and velocity components, respectively and u_i', p' and ρ' are the fluctuating velocity, pressure and density about these incompressible variables, respectively. Introducing the decomposed variables into the compressible Navier–Stokes equations, the final perturbed equations read

$$\frac{\partial \rho'}{\partial t} + \frac{\partial f_i}{\partial x_i} = 0, \tag{4}$$

$$\frac{\partial f_i}{\partial t} + \frac{\partial}{\partial x_j}[f_i(U_j + u_j') + \rho_0 U_i u_j' + p'\delta_{ij}] = \frac{\partial \tau_{ij}'}{\partial x_j}, \tag{5}$$

$$\frac{\partial p'}{\partial t} - c^2 \frac{\partial \rho'}{\partial t} = -\frac{\partial P}{\partial t}, \tag{6}$$

where the acoustic co-velocity components $f_i = \rho u_i' + \rho' U_i$ and perturbed viscous stresses $\tau_{ij}' = \mu(\partial u_i'/\partial x_j + \partial u_j'/\partial x_i - \frac{2}{3}\delta_{ij}\partial u_k'/\partial x_k)$. In contrast to the former inviscid formulation, the viscous stresses are retained in Eq. (5). Apart from modeling correctly the influence of viscosity, this greatly simplifies the treatment of the boundary conditions. In fact, the extrapolation needed for the boundary equations in an inviscid formulation on a non-staggered mesh leads to spurious noise sources, especially near-sharp edges.

The diffusion terms can be expressed in terms of the acoustic co-variable f_i,

$$\tau_{ij}' = \frac{\mu}{\rho}\left(\frac{\partial f_i}{\partial x_j} + \frac{\partial f_j}{\partial x_i}\right) - r_{ij}, \tag{7}$$

$$r_{ij} = \frac{\mu}{\rho}\left[(u_i' + U_i)\frac{\partial \rho'}{\partial x_j} + \rho'\frac{\partial U_i}{\partial x_j} + (u_j' + U_j)\frac{\partial \rho'}{\partial x_i} + \rho'\frac{\partial U_j}{\partial x_i} + \frac{2}{3}\rho\delta_{ij}\frac{\partial u_k'}{\partial x_k}\right]. \tag{8}$$

The acoustic sources are computed by the incompressible equations and the viscous term in the perturbed equations is used to stabilize the inviscid perturbed equations.

Closure of the formulation is accomplished by the approximation that, for a general airflow,

$$c^2 = \frac{\gamma p}{\rho} = \frac{\gamma(P + p')}{\rho_0 + \rho'},$$

where $\gamma = 1.4$ is the ratio of specific heats.

Now we consider the boundary conditions. At the far-field of the computational domain, the 2D acoustic waves can be considered as cylindrical waves and the leading terms may be written in the form, $f(r - (u_n + c)t, \theta)/\sqrt{r}$, where n is the normal direction out of the domain, $u_n = \vec{u} \cdot \vec{n}$, and r is the distance between the far-field boundary and the body center. For more details, the reader is referred to Tam and Webb [8]. The boundary conditions become

$$\frac{\partial \rho'}{\partial t} + (c + u_n)\left(\frac{\partial \rho'}{\partial n} + \frac{\rho'}{2r}\right) = 0, \tag{9}$$

$$\frac{\partial u_i'}{\partial t} + (c + u_n)\left(\frac{\partial u_i'}{\partial n} + \frac{u_i'}{2r}\right) = 0, \tag{10}$$

$$\frac{\partial p'}{\partial t} + (c + u_n)\left(\frac{\partial p'}{\partial n} + \frac{p'}{2r}\right) = 0. \tag{11}$$

At outflow boundaries, where the acoustic waves are combined with vorticity waves, the acoustic velocity boundary conditions are changed as

$$\frac{\partial u_i'}{\partial t} + u_n \frac{\partial u_i'}{\partial n} + \frac{1}{\rho_0}\frac{\partial p'}{\partial x_i} = 0. \tag{12}$$

At wall boundaries, boundary conditions for inviscid perturbed equations are

$$\vec{u}' \cdot \vec{n} = 0 \quad \text{or} \quad \vec{f} \cdot \vec{n} = 0, \tag{13}$$

$$\frac{\partial p'}{\partial n} = -\frac{f_\tau(U_\tau + u_\tau') + \rho_0 U_\tau u_\tau'}{R} = -\frac{\rho(u_\tau')^2}{R}, \tag{14}$$

where $\vec{\tau}$ is the tangential direction and R is the radius of curvature. The boundary condition for ρ' is extrapolated from interior points.

The wall boundary conditions for viscous perturbed equations are no-slip conditions ($\vec{u}' = 0$ or $\vec{f} = 0$). The boundary conditions for ρ' and p' are extrapolated from interior points.

3. Numerical discretization

The numerical discretization for both the incompressible flow equations and the perturbed equations is based on a cell-centered finite volume method, which is second order accurate in time and space $O(\delta t^2, \delta x^2)$. The incompressible flow equations are solved by the cell-centered finite-volume/multi-block based code EllipSys. For further details, the reader is referred to Michelsen [19] and Sørensen [20]. In this section, we consider the discretization of the perturbed equations. The perturbed equations can be discretized using the SIMPLE method in [17] or the SIMPLEC method in [18]. Here we describe only the SIMPLE method. It consists of a predictor and a corrector step, as shown in the following.

3.1. Predictor step

The acoustic momentum equations, Eq. (5), are discretized at time level $(n + 1/2)\delta t$ using a second-order semi-implicit Crank–Nicolson scheme in time for both convection and normal diffusion terms. The spatial resolution is based on a second-order central difference scheme for the diffusion terms and the QUICK upwinding scheme for the convection terms. The resulting equations for each cell can be written as

$$\left(\frac{2J}{\delta t} + A_P\right) f_{x,P}^* + \sum_{\text{EWNS}} A_i f_{x,i}^* = \left(\frac{2J}{\delta t} - A_P\right) f_{x,P}^n - \sum_{\text{EWNS}} A_i f_{x,i}^n + 2S_{x,P}^{n+1/2} - 2y_\eta p_\xi'^{,n} + 2y_\xi p_\eta'^{,n}, \tag{15}$$

$$\left(\frac{2J}{\delta t} + A_P\right) f_{y,P}^* + \sum_{\text{EWNS}} A_i f_{y,i}^* = \left(\frac{2J}{\delta t} - A_P\right) f_{y,P}^n - \sum_{\text{EWNS}} A_i f_{y,i}^n + 2S_{y,P}^{n+1/2} + 2x_\eta p_\xi'^{,n} - 2x_\xi p_\eta'^{,n}, \tag{16}$$

where (x, y) are Cartesian coordinates and (ξ, η) are curvilinear coordinates, A_P and A_i are the coefficients from the spatial discretization of convection and normal diffusion, and the compass summation notation, $\sum_{\text{EWNS}}$, is adopted. For convenience, the mapping from the physical Cartesian domain (x, y) to the

computational domain (ξ,η) is chosen such that $\delta\xi = \delta\eta = 1$. The acoustic pressure forces acting on a cell of volume J are tentatively evaluated at prior time t^n. $S^{n+1/2}$ contains the remaining acoustic momentum terms including the source term $\partial(\rho_0 U_i u_j')/\partial x_j$ and the remaining term from the diffusion and is discretized by using Adams–Bashforth extrapolation. Solution of Eqs. (15) and (16) yields intermediate acoustic co-velocity components $(f_{x,P}^*, f_{y,P}^*)$, which do not satisfy acoustic mass conservation, Eq. (4).

3.2. Corrector step

The acoustic pressure at time level $(n+1)\delta t$ may be expressed as a correction $p'^{,n+1} = p'^{,n} + \alpha_p p''$ where α_p is the under-relaxation parameter for pressure. From the heuristic analysis of Ferziger and Peric [21], the under-relaxation parameter has no global optimal value for unsteady computations and the value differs from point to point. For convenience, α_p is set equal to unity as for the unsteady SIMPLEC scheme. The acoustic co-velocity components are corrected as

$$f_x^{n+1} = f_x^* + f_x' = f_x^* - (y_\eta/A_P^*)p_\xi'' + (y_\xi/A_P^*)p_\eta'', \tag{17}$$

$$f_y^{n+1} = f_y^* + f_y' = f_y^* + (x_\eta/A_P^*)p_\xi'' - (x_\xi/A_P^*)p_\eta'', \tag{18}$$

where $A_P^* = A_P + 2J/\delta t$. For notation simplicity, an orthogonal mesh is considered.

In order to drive the pressure correction equation, we consider the mass conservation, Eq. (4), and correlation equation, Eq. (6), together. We get

$$\frac{1}{c^2}\frac{\partial p'}{\partial t} + \frac{\partial f_i}{\partial x_i} = -\frac{1}{c^2}\frac{\partial P}{\partial t}. \tag{19}$$

Inserting the pressure correction and acoustic co-velocity corrections, Eqs. (17) and (18), the pressure correction equation is obtained:

$$\frac{Jp''}{c^2\delta t} + \frac{\partial}{\partial\xi}\left(\frac{B}{A_P^*}\frac{\partial p''}{\partial\xi}\right) + \frac{\partial}{\partial\eta}\left(\frac{C}{A_P^*}\frac{\partial p''}{\partial\eta}\right) = -\frac{J(P^{n+1}-P^n)}{c^2\delta t} - \sum_{e,w,n,s} G_i^*, \tag{20}$$

where $B = -(x_\eta^2 + y_\eta^2)$ and $C = -(x_\xi^2 + y_\xi^2)$. The mass flux across the cell faces, G^*, is computed as

$$G_e^* = \overline{\left(\frac{2J/\delta t - A_P}{A_P^*}\right)}\,|_e\; G_e^n + \overline{H_e} + \overline{\left(\frac{B}{A_P^*}\right)}\,|_e\;(p_E'^{,n} - p_P'^{,n}), \tag{21}$$

where H is the flux computed from the auxiliary acoustic co-velocity $(\hat{f}_x, \hat{f}_y)$

$$\hat{f}_{x,P} = -\sum_{\mathrm{EWNS}} \frac{A_i}{A_P^*}(f_{x,i}^* + f_{x,i}^n) + \frac{2S_{x,P}^{n+1/2}}{A_P^*}, \tag{22}$$

$$\hat{f}_{y,P} = -\sum_{\mathrm{EWNS}} \frac{A_i}{A_P^*}(f_{y,i}^* + f_{y,i}^n) + \frac{2S_{y,P}^{n+1/2}}{A_P^*}. \tag{23}$$

After the acoustic pressure has been corrected, the acoustic density is updated from

$$\rho'^{,n+1} = \rho'^{,n} + \frac{p'^{,n+1} + P'^{,n+1} - p'^{,n} - P'^{,n}}{1.5c^2\,|^n - 0.5c^2\,|^{n-1}}. \tag{24}$$

The acoustic velocity is obtained through the definition of acoustic co-velocity f_i:

$$u_i'^{,n+1} = \frac{f_i^{n+1} - \rho'^{,n+1} U_i^{n+1}}{\rho_0 + \rho'^{,n+1}}. \tag{25}$$

The acoustic sound speed is computed by

$$c^{n+1} = \sqrt{\frac{\gamma(P^{n+1} + p'^{,n+1})}{\rho_0 + \rho'^{,n+1}}}. \tag{26}$$

3.3. Grid arrangement

The flow solver EllipSys is a parallelized CFD code based on multi-block strategy. In order to exploit the power of parallel computing, the acoustic part is parallelized in the same way as the flow solver. As the physical behavior of fluid flow and acoustic waves are different, different mesh strategies are utilized. A mesh resolving well viscous flows has concentrated points in the viscous boundary layer and wakes, and few points or coarse points in the rest of domain. In contrast, to describe acoustic waves, relatively more points are needed in the far-field. On the other hand, a less concentrated distribution of mesh points in the viscous boundary layer is needed. After generating a mesh for flow computations, the acoustic mesh can be obtained making the following transformations to the flow mesh: (a) in near-wall blocks the mesh is moved a little away from the wall region into outer region, in other words the mesh stretching is reduced; (b) in far-field blocks the points are mapped and concentrated in a relatively smaller region, and/or additional blocks in the far-field are added.

4. Numerical results and discussion

In the following, the described method is applied for laminar flows past a circular cylinder and a NACA 0015 airfoil at Mach number $M = 0.2$, and for laminar airfoil flows interacting with a vortical gust at Mach number $M = 0.5$.

4.1. Cylinder flow

In this section, the flow past a circular cylinder at Reynolds number $Re = 200$ and $M = 0.2$ is considered. This flow has previously been computed using a staggered method [14]. The computational region for both incompressible and acoustic computations ranges 45 cylinder diameters away from the cylinder, and is covered by an O-mesh consisting of 192 cells in tangential direction and 128 cells in radial direction (i.e. 192×128). The mesh is equidistant in the tangential direction and stretched in the radial direction. The dimensionless time step is $\delta t = 0.0025$, based on cylinder diameter and free-stream velocity.

The incompressible computation is started before the acoustic computation. After a non-dimensional time of $t = 200$, an incompressible periodic state is fully established. The lift force of the incompressible solution computed on the original mesh (OM) of 192×128 is compared to that obtained on a finer mesh (FM) with double as many mesh points in each direction, 384×256. The difference in amplitude, defined as $[(:)_{\mathrm{FM}} - (:)_{\mathrm{OM}}]/(:)_{\mathrm{FM}}$, is 3.6%. The frequency obtained on the fine mesh is 0.195 whereas the one from the OM is 0.1922. The difference is 1.436%. The same phenomenon is seen in the drag plot (not shown). The difference of mean drag force is 0.23%.

From this we conclude that the OM is sufficient for resolving the flow field.

4.1.1. Inviscid acoustic computations

To compare the viscous model with the former inviscid model on collocated grids, we first perform inviscid acoustic computations with slip boundary conditions. Normalized fluctuating pressure $(p - p_0)/p_0$ at $(x, y) = (0, 20)$ computed on the OM is plotted in Fig. 1. The acoustic pressure becomes periodic after $t = 500$. The signal is dominated by the Strouhal frequency, but a small irregularity is seen. The mean amplitude of the signal is about 20% higher than that obtained using the staggered method [14]. In order to judge the quality of the computational results, an additional computation on the fine mesh is carried out. The normalized fluctuating pressure at the same position is plotted in Fig. 2. The signal is still dominated by the basic Strouhal frequency, but a stronger irregularity of the acoustic pressure is clearly seen.

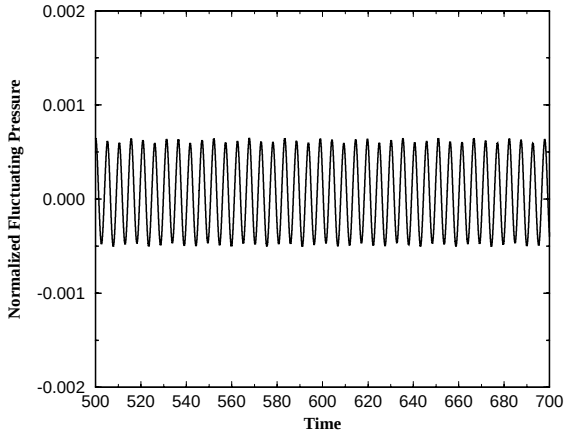

Fig. 1. Normalized fluctuating pressure $(p - p_0)/p_0$ at $(x, y) = (0, 12)$ for laminar flow past a circular cylinder at $Re = 200$ and $M = 0.2$. Inviscid acoustic computation on a mesh of 192×128.

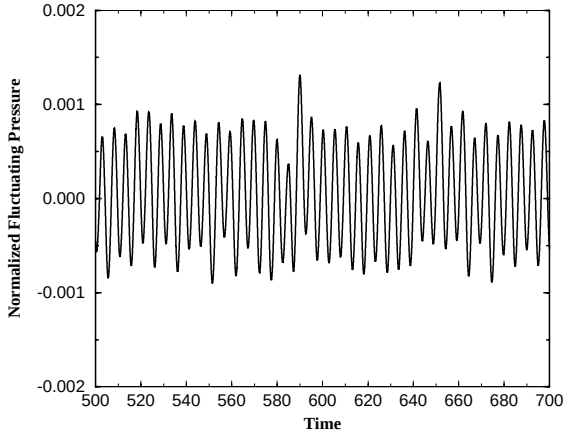

Fig. 2. Normalized fluctuating pressure $(p - p_0)/p_0$ at $(x, y) = (0, 12)$ for laminar flow past a circular cylinder at $Re = 200$ and $M = 0.2$. Inviscid acoustic computation on a mesh of 384×256.

4.1.2. Viscous acoustic computations

Viscous acoustic computations with no-slip boundary conditions are now performed. The normalized fluctuating pressure $(p - p_0)/p_0$ at $(x, y) = (0, 20)$ computed on the OM is plotted in Fig. 3. The acoustic pressure becomes periodic after $t = 500$. Comparing to the inviscid result (Fig. 1), the acoustic signal is more regular. In order to quantify the grid dependency, computations are performed on the FM. The normalized fluctuating pressure at the same position is plotted in Fig. 4. Comparing the signal with the one obtained on the OM, the amplitude is seen to be increased by 1.35%, which is almost the same amplitude as that obtained by the staggered method [14]. Moreover, the acoustic solution now becomes periodic on the fine mesh.

The acoustic pressure is plotted in Fig. 5. From the figure, the acoustic waves are seen to propagate preferably from the cylinder along the normal direction of the flow. There are about two crests in the

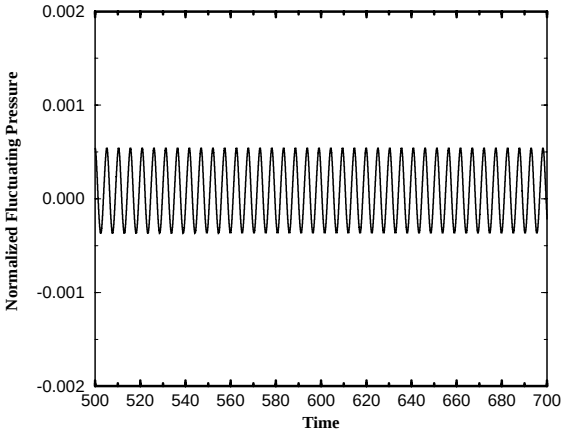

Fig. 3. Normalized fluctuating pressure $(p - p_0)/p_0$ at $(x, y) = (0, 12)$ for laminar flow past a circular cylinder at $Re = 200$ and $M = 0.2$. Viscous acoustic computation on a mesh of 192×128.

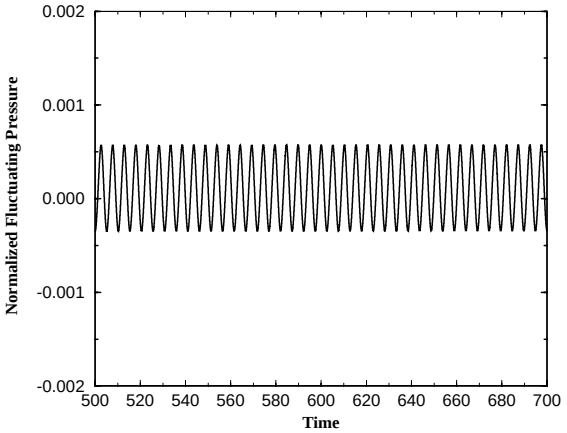

Fig. 4. Normalized fluctuating pressure $(p - p_0)/p_0$ at $(x, y) = (0, 12)$ for laminar flow past a circular cylinder at $Re = 200$ and $M = 0.2$. Viscous acoustic computation on a mesh of 384×256.

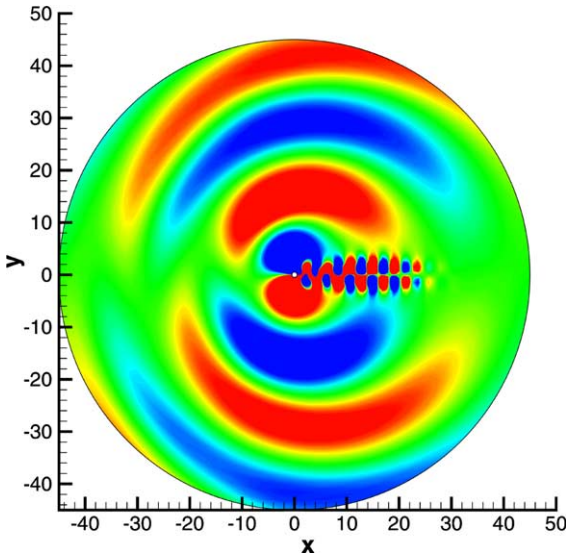

Fig. 5. Instantaneous plot of fluctuating pressure, p', for laminar flow past a circular cylinder at $Re = 200$, $M = 0.2$ and $t = 700$.

normal direction of the computational domain that corresponds to about 64 grid points per wavelength on the average. The directivity pattern of the cylinder noise radiation at $M = 0.2$, measured at a distance $d = 20$ diameters from the cylinder center, is shown in Fig. 6. From the figure, the radiation is symmetric and a peak radiation in the cylinder wake, corresponding to the vorticity wave can be seen. The levels range from 100 to 124 dB with a reference of 2×10^{-5} Pa.

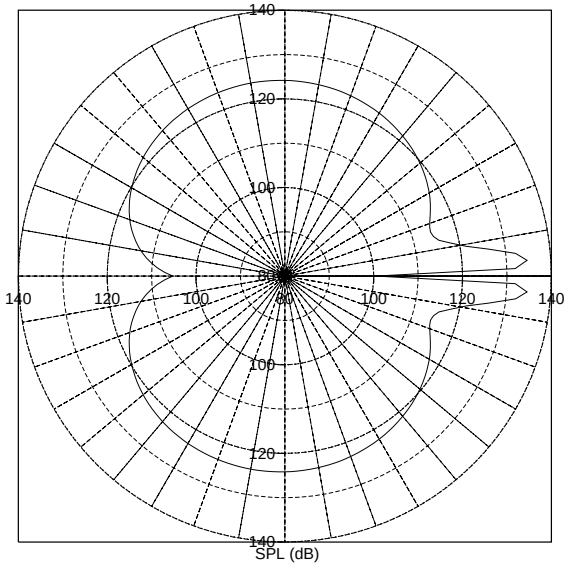

Fig. 6. Directivity pattern of circular cylinder noise radiation at $Re = 200$, $M = 0.2$ and $d = 20$.

4.2. Airfoil flow

In order to analyze acoustic waves generated by vortex shedding from an airfoil, laminar flow past a NACA 0015 airfoil at $Re = 300$, incidence 20° and $M = 0.2$ is computed. The incompressible solution is calculated on a 192×128 O-grid generated by conformal mapping in a domain of radius equal to about 50 chord lengths. The acoustic solution is performed on an O-grid consisting of 192×128 cells in a domain of radius equal to about 25 chord lengths. The acoustic mesh has less points in the airfoil boundary region and more points in the far-field. The dimensionless time step is $\delta t = 0.0004$, based on airfoil chord and free-stream velocity.

The incompressible computation is again started before the acoustic computation to eliminate acoustic transients. After a dimensionless time of $t = 80$, an incompressible periodic state is fully established. The lift force of the incompressible solution computed on the OM of 192×128 is compared to that obtained on a FM with double as many mesh points in each direction, 384×256. The mean value of lift computed on the fine mesh is 0.3756. The difference in mean lift between the fine and OMs, defined as $[(:)_{\mathrm{FM}} - (:)_{\mathrm{OM}}]/(:)_{\mathrm{FM}}$, is 1.98%. The difference in lift amplitude is 10.8%. The frequency obtained on the

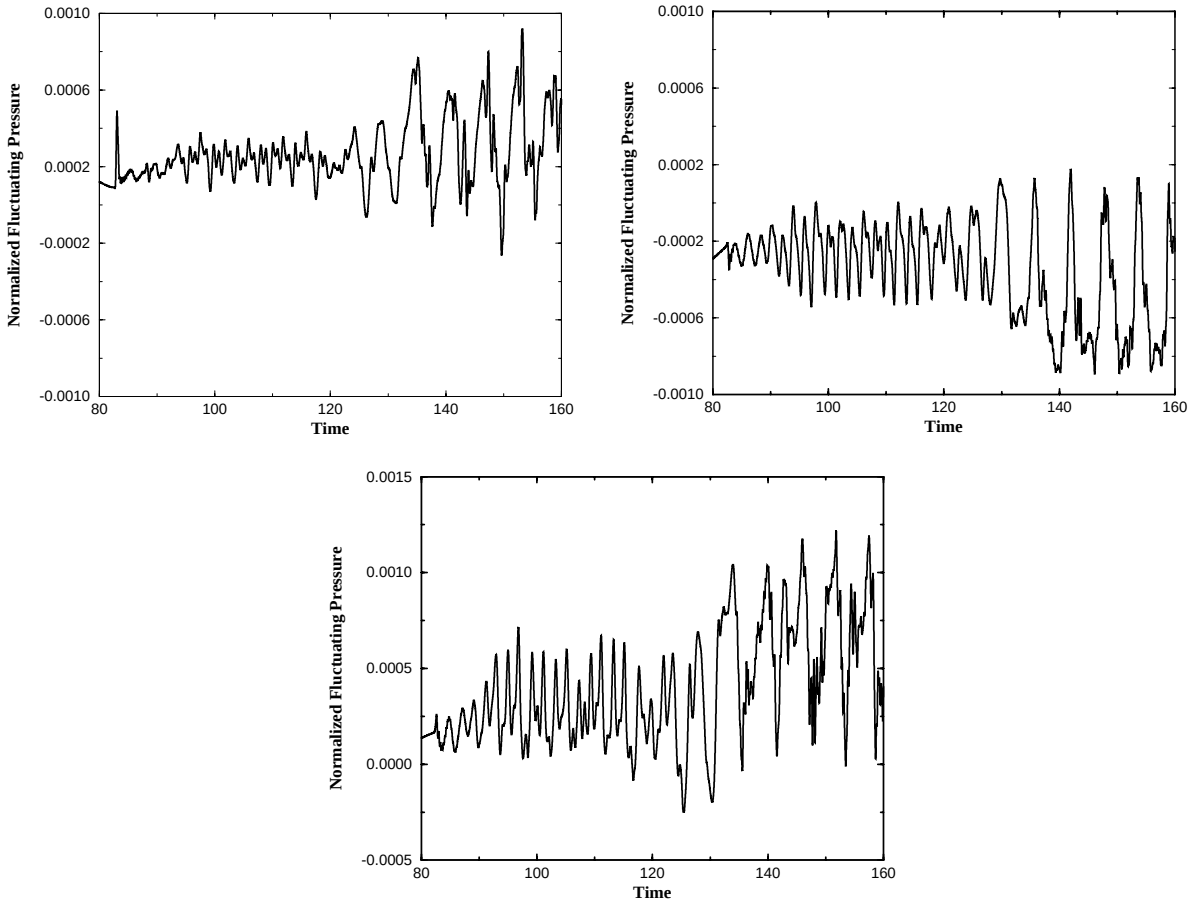

Fig. 7. Normalized pressure $(p - p_0)/p_0$ at $r = 12$ for laminar flow past a NACA 0015 airfoil at $Re = 300$, incidence 20° and $M = 0.2$, measured at $(x, y) = (12, 0)$, (0,12) and $(0, -12)$. Inviscid acoustic computation on a mesh of 192×128.

fine mesh is 0.435 whereas the one from the OM is 0.427. The difference is 1.84%. The same phenomenon is seen in the drag plot. The difference of mean drag force is 0.05%.

From this we conclude that the OM is sufficient for resolving the flow field.

4.2.1. Inviscid acoustic computations

To compare the viscous model with the former inviscid model on collocated grids, we first perform inviscid acoustic computations with slip boundary conditions. Normalized fluctuating pressure $(p - p_0)/p_0$ at $(x, y) = (12, 0)$, $(0, 12)$ and $(0, -12)$ computed on the OM is plotted in Fig. 7. From the figure, an amplification of the acoustic pressure is seen. At the beginning of the acoustic computation, the Strouhal frequency is found. Later, the acoustic solution becomes irregular due to interpolation errors at wall boundaries.

4.2.2. Viscous acoustic computations

Viscous acoustic computations with no-slip boundary conditions are now performed. The normalized fluctuating pressure $(p - p_0)/p_0$ at $(x, y) = (12, 0)$, $(0, 12)$ and $(0, -12)$ computed on the OM is plotted in

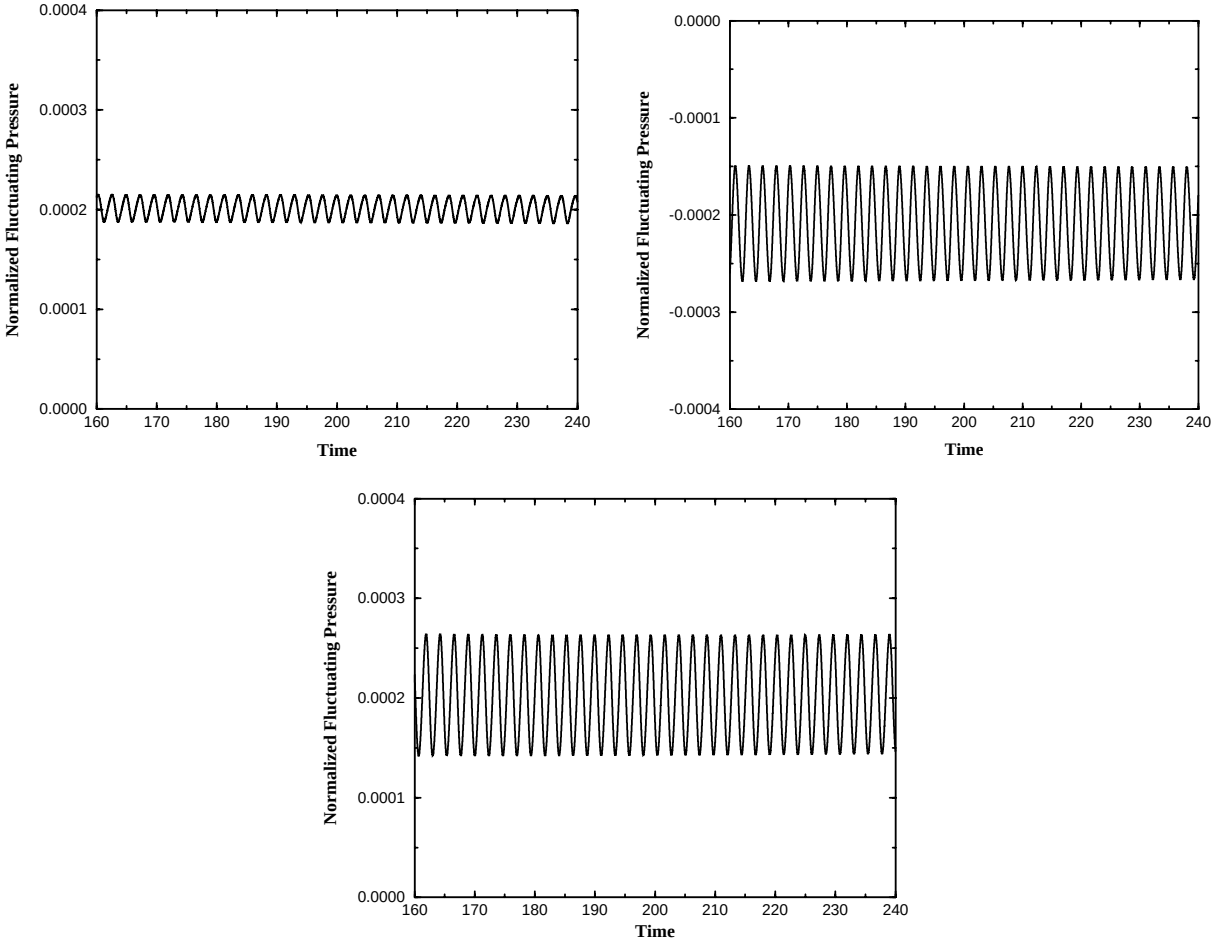

Fig. 8. Normalized pressure $(p - p_0)/p_0$ at $r = 12$ for laminar flow past a NACA 0015 airfoil at $Re = 300$, incidence 20° and $M = 0.2$, measured at $(x, y) = (12, 0)$, (0,12) and (0,−12). Viscous acoustic computation on a mesh of 192×128.

Fig. 8. The acoustic pressure becomes periodic after $t = 160$. Comparing the acoustic signal with the one obtained in [15], the pressure signal has the same order of magnitude. In order to quantify the grid dependency, computations are performed on the fine mesh. The normalized fluctuating pressure at the same positions is plotted in Fig. 9. Comparing the signal computed with the one obtained on the OM, the amplitude is seen to be increased by 9.15%.

The acoustic pressure is plotted in Fig. 10. From the figure, the waves are moving in the normal direction away from the airfoil surface. Due to the waves being generated mainly by the vortex shedding process, waves move at opposite phase on the upper and lower side. Hence, at a direction of approximately 10°, the acoustic waves are extinguished. There are about three crests in the normal direction of the computational domain that corresponds to about 43 grid points per wavelength on the average. The directivity pattern of the cylinder noise radiation at $M = 0.2$, measured at a distance $d = 12$ chords from the airfoil center, is shown in Fig. 11. From the figure, the radiation is symmetric about the line of about 10° before the airfoil and almost symmetric about the inflow direction in the wakes. A peak radiation in

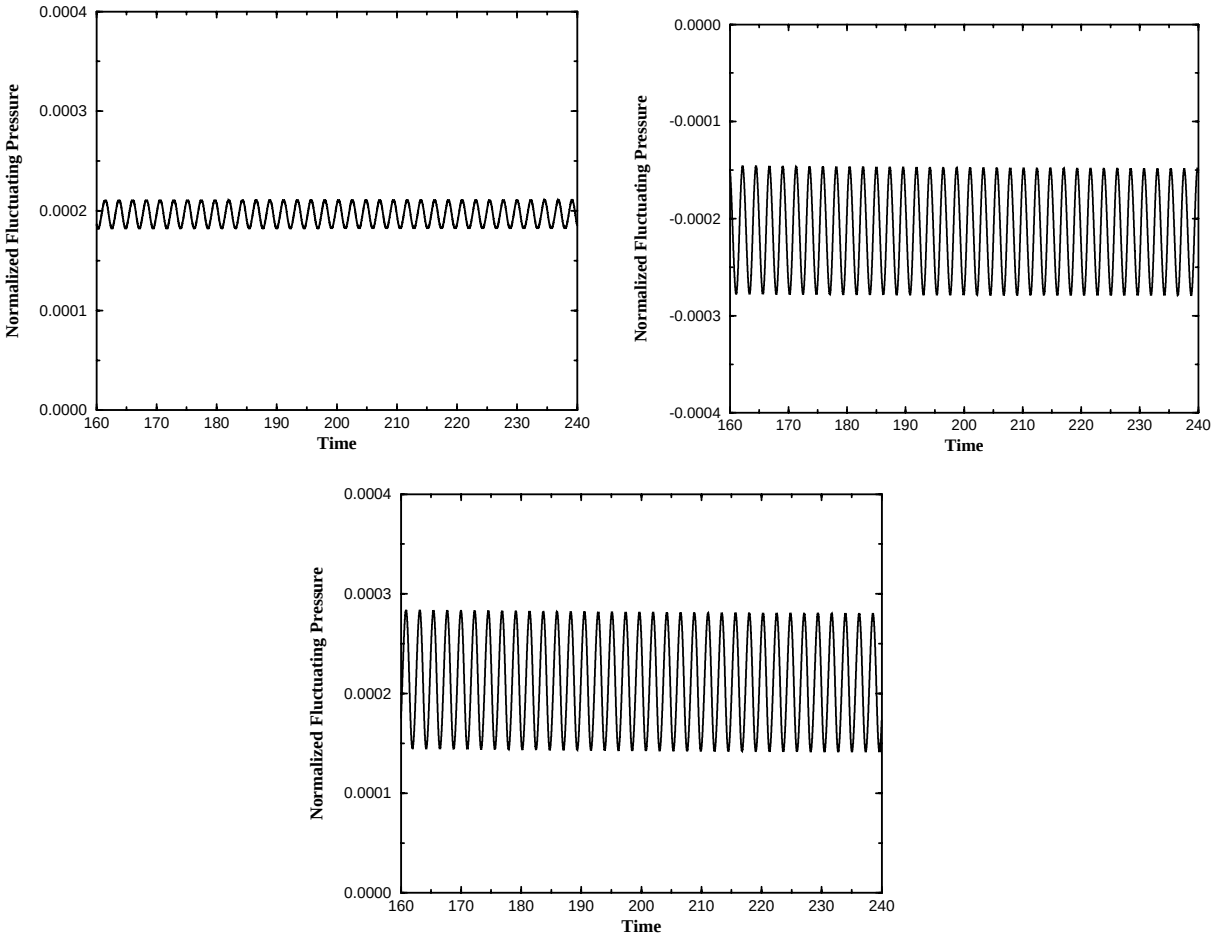

Fig. 9. Normalized pressure $(p - p_0)/p_0$ at $r = 12$ for laminar flow past a NACA 0015 airfoil at $Re = 300$, incidence 20° and $M = 0.2$, measured at $(x, y) = (12, 0)$, (0,12) and $(0, -12)$. Viscous acoustic computation on a mesh of 384×256.

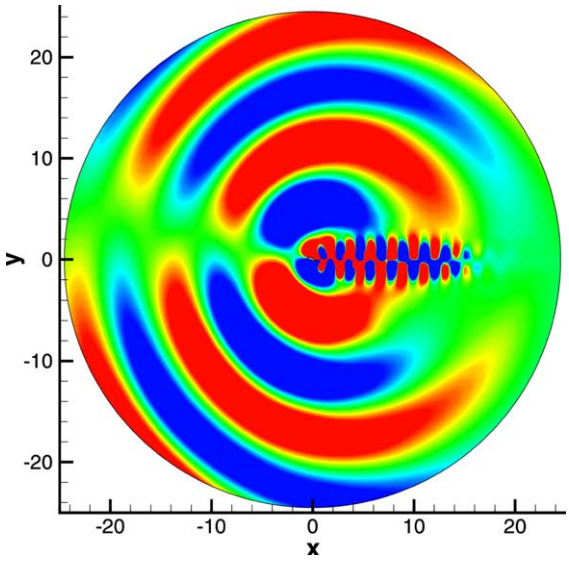

Fig. 10. Instantaneous plot of fluctuating pressure, p', for laminar flow past a NACA 0015 airfoil at $Re = 300$, $M = 0.2$ and $t = 240$.

the airfoil wake, corresponding the vorticity wave can be easily seen. The levels range from 78 to 108 dB with a reference of 2×10^{-5} Pa.

4.3. Airfoil–Gust interaction

The interaction of a vortical gust with a finite thickness airfoil represents an important issue for methods of broadband airfoil noise prediction. The vortical gust problem has previously been studied by Scott and

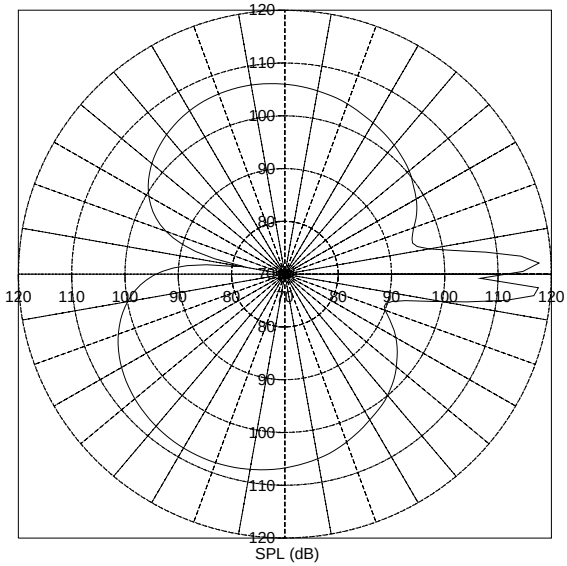

Fig. 11. Directivity pattern of NACA 0015 noise radiation at $Re = 300$, $M = 0.2$ and $d = 12$.

Atassi [22], and Lockard and Morris [23]. In order to compare with the results obtained by Lockard and Morris [23], a plane vortical disturbance of the form

$$v = a_1 U_\infty \cos[\omega(x - U_\infty t)], \tag{27}$$

is introduced. Since the gust is essentially vortical and incompressible, the source function is included to the incompressible equations. When the governing equations are non-dimensionalized with free-stream velocity U_∞ and airfoil chord c, the incompressible equations are modified to include source terms in the form

$$\frac{\partial u}{\partial t} \ldots = \frac{\partial \Psi}{\partial y} \sin(2kt), \tag{28}$$

$$\frac{\partial v}{\partial t} \ldots = -\frac{\partial \Psi}{\partial x} \sin(2kt), \tag{29}$$

where

$$\Psi = a_1 \frac{b^2 - 4k^2}{4b^2 \sin(2k\pi/b)} \{1 + \cos[b(x - x_0)]\}\{\tanh[6(y + y_0)] - \tanh[6(y - y_0)]\}, \tag{30}$$

defined in the range $| x - x_0 | \leqslant \pi/b$, where (x_0, y_0) is the center of the source, b specifies its width and $k = \omega c/(2U_\infty)$.

In the present paper, a gust is produced using the following parameters:

$$a_1 = 0.002, \qquad b = 10,$$

$$x_0 = -1.25, \qquad y_0 = 0.75.$$

In the following, viscous computations of flows past a NACA 0012 airfoil at Reynolds number $Re = 5000$, Mach number $M = 0.5$ and incidence 0° are carried out at a low frequency of $k = 1$ and a high frequency of $k = 7.85$.

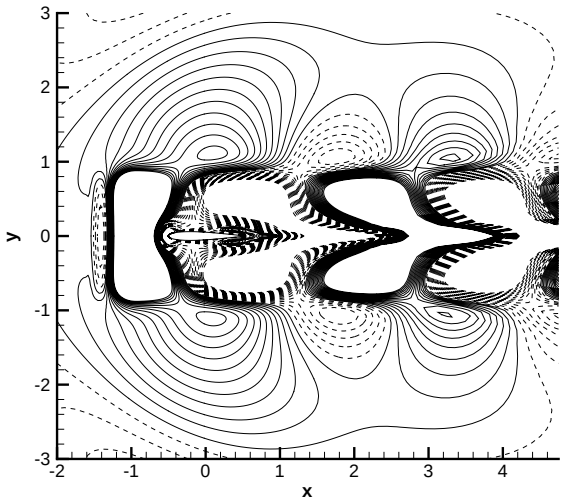

Fig. 12. Instantaneous $v - \bar{v}$ plot for a NACA 0012 airfoil; $k = 1$, $M = 0.5$, $Re = 5000$ and $\alpha = 0°$.

4.3.1. Low frequency

A reduced frequency of $k = 1$ is used as a first test case. Both incompressible and acoustic computations are based on the same O-mesh consisting of 256 cells in tangential direction and 192 cells in radial direction, located in a domain of about 10 airfoil chords.

Once the incompressible solution with the gust is established, the acoustic computation is started. In order to get an impression of the gust, a plot of the fluctuating vertical velocity component $v - \bar{v}$, where $\bar{v}$ is the time–average velocity, is shown in Fig. 12. From the figure, a low frequency gust is seen, which interacts with the airfoil. Due to the influence of the airfoil and viscosity, the gust form is changed in the airfoil wake. In the plot, a small velocity fluctuation of acoustic waves is observed. In Fig. 13, the directivity of the perturbation pressure normalized by $\rho_\infty U_\infty a_1$, is plotted and compared to the results of Lockard and Morris [23]. Comparing the plots, the directivity of our viscous computations is seen to be closer to their inviscid one. In the following, $|p'|$ denotes the amplitude of p'. For 2D flows, the magnitude $\sqrt{r}\,|p'|$ is

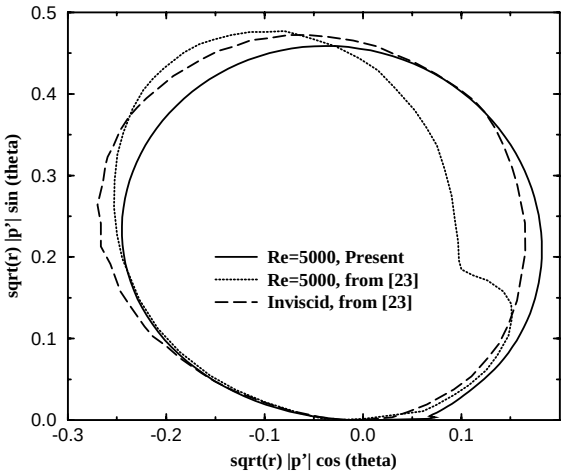

Fig. 13. Directivity variation for a NACA 0012 airfoil; $k = 1$, $M = 0.5$, $Re = 5000$ and $\alpha = 0°$.

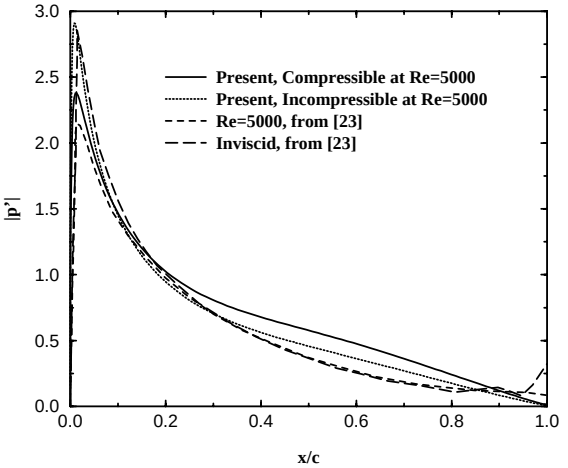

Fig. 14. Surface pressure magnitude variation for a NACA 0012 airfoil; $k = 1$, $M = 0.5$, $Re = 5000$ and $\alpha = 0°$.

almost constant at distances far away from the airfoil. In the present computation, a distance of three airfoil-chords is chosen to get the directivity plot. The distribution of normalized surface pressures are plotted in Fig. 14. A slightly higher surface fluctuation is seen in the middle of the airfoil, as compared to the viscous and inviscid pressure magnitudes in [23]. Finally, in Fig. 15 a fluctuating pressure is plotted which shows the acoustic waves generated from the airfoil interacting with the gust.

4.3.2. High frequency

As next test case, a higher reduced frequency of $k = 7.85$ is used. Both incompressible and acoustic computations are based on a fine O-mesh, consisting of 512 cells in tangential direction and 384 cells in radial direction, located in a domain of about 10 airfoil chords.

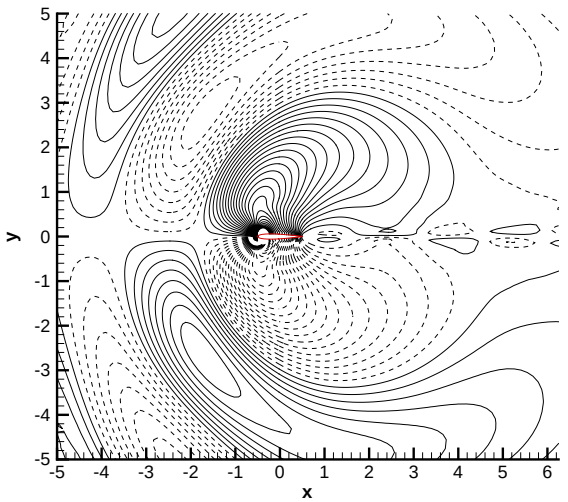

Fig. 15. Instantaneous $p - \bar{p}$ plot for a NACA 0012 airfoil; $k = 1$, $M = 0.5$, $Re = 5000$ and $\alpha = 0°$.

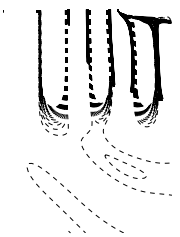

Once the incompressible solution with the gust is established, the acoustic computation is started. A plot of the fluctuating vertical velocity component, $v - \bar{v}$, is shown in Fig. 16. From the figure, it is seen that a high frequency gust is generated and interacts with the airfoil. As in the low-frequency case, a small velocity fluctuation due to acoustic waves is seen in the near-field. Compared to Fig. 6 in Lockard and Morris [23], a small difference is seen in the airfoil wake due to the presence of viscosity. In Fig. 17, the directivity is plotted and compared to the results of Lockard and Morris [23]. The comparisons are in good agreement for $x > 0$, but is under-predicted when $x < 0$. This is because the gust is generated after the position $x = -1.25$. In order to include the gust in the directivity, a plot of $r/c = 1$ is also added in the figure. Overall the results are comparable to the inviscid directivity of [23]. Absolute values of normalized surface pressures are plotted in Fig. 18. The magnitude of the surface pressure is close to the inviscid result in [23]. Finally, a fluctuating pressure is plotted in Fig. 19 which shows the acoustic waves generated from the airfoil interacting with the gust.

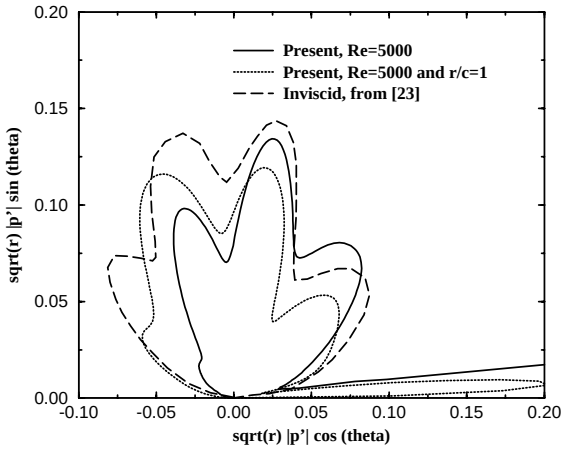

Fig. 17. Directivity variation for a NACA 0012 airfoil; $k = 7.85$, $M = 0.5$, $Re = 5000$ and $\alpha = 0°$.

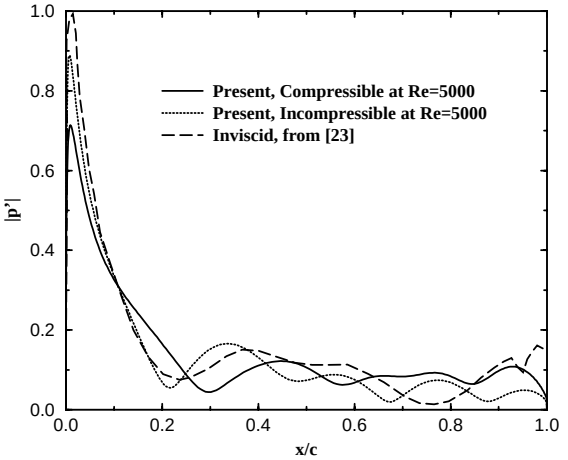

Fig. 18. Surface pressure magnitude variation for a NACA 0012 airfoil; $k = 7.85$, $M = 0.5$, $Re = 5000$ and $\alpha = 0°$.

[4] F. Farassat, K.S. Brentner, The uses and abuses of the acoustic analogy in helicopter rotor noise prediction, Journal of the American Helicopter Society 33 (1) (1988) 29.
[5] F. Farassat, G.P. Succi, The prediction of helicopter discrete frequency noise, Vertica 7 (4) (1983) 309.
[6] J.B. Freund, A simple method for computing far-field sound in aeroacoustic computations, Journal of Computational Physics 157 (2000) 796.
[7] J.S. Cox, K.S. Brentner, C.L. Rumsey, Computation of vortex shedding and radiated sound for a circular cylinder: subcritical to transcritical Reynolds numbers, Theoretical and Computational Fluid Dynamics 12 (1998) 233.
[8] C.K.W. Tam, J.C. Webb, Dispersion relation preserving finite difference schemes for computational acoustics, Journal of Computational Physics 107 (1993) 262.
[9] H. Shen, C.K.W. Tam, Numerical simulation of the generation of axisymmetric mode jet screech tones, AIAA Journal 36 (10) (1998) 1801.
[10] S.A. Slimon, M.C. Soteriou, D.W. Davis, Development of computational aeroacoustics equations for subsonic flows using a Mach number expansion approach, Journal of Computational Physics 159 (2000) 377.
[11] J.C. Hardin, D.S. Pope, An acoustic/viscous splitting technique for computational aeroacoustics, Theoretical and Computational Fluid Dynamics 6 (5–6) (1994) 323.
[12] J.A. Ekaterinaris, New formulation of Hardin–Pope equations for aeroacoustics, AIAA Journal 37 (9) (1999) 1033.
[13] W.Z. Shen, J.N. Sørensen, Comment on the aeroacoustic formulation of Hardin and Pope, AIAA Journal 37 (1) (1999) 141.
[14] W.Z. Shen, J.N. Sørensen, Aeroacoustic formulation of low-speed flows, Theoretical and Computational Fluid Dynamics 13 (1999) 271.
[15] W.Z. Shen, J.N. Sørensen, Aeroacoustic modeling of turbulent airfoil flows, AIAA Journal 39 (6) (2001) 1057.
[16] C.M. Rhie, W.L. Chow, Numerical study of the turbulent flow past an airfoil with trailing edge separation, AIAA Journal 21 (11) (1983) 1525.
[17] W.Z. Shen, J.A. Michelsen, J.N. Sørensen, Improved Rhie-Chow interpolation for unsteady flow computations, AIAA Journal 39 (12) (2001) 2406.
[18] W.Z. Shen, J.A. Michelsen, N.N. Sørensen, J.N. Sørensen, An improved SIMPLEC method for steady and unsteady flow computations, Numerical Heat Transfer 43 (3) (2003) 221.
[19] J.A. Michelsen, Basis3D – A Platform for Development of Multiblock PDE Solvers, Technical Report AFM 92-05, Technical University of Denmark, Denmark, 1992.
[20] N.N. Sørensen, General Purpose Flow Solver Applied Over Hills, RISØ-R-827-(EN), Risø National Laboratory, Roskilde, Denmark, 1995.
[21] J.H. Ferziger, M. Peric, Computational Methods for Fluid Dynamics, Springer-Verlag, Berlin, Heidelberg, 1996.
[22] J.R. Scott, H.M. Atassi, A finite-difference, frequency-domain numerical scheme for the solution of the gust response problem, Journal of Computational Physics 119 (1995) 75.
[23] D.P. Lockard, P.J. Morris, Radiated noise from airfoils in realistic mean flows, AIAA Journal 36 (6) (1998) 907.